

HCHO in a Cold, Quantum Solvent: Size and Shape of Its “Bubbles” in ^4He Droplets from Stochastic Simulations[†]

F. Marinetti,[‡] E. Yurtsever,[§] and F. A. Gianturco^{*,‡}

Department of Chemistry and CNISM, University of Rome La Sapienza, Piazzale A. Moro 5, 00185 Rome, Italy, and Department of Chemistry, Koç, University, Rumelifeneriyolu, 34450 Sariyer, Istanbul, Turkey

Received: March 2, 2010; Revised Manuscript Received: April 23, 2010

The full interaction between formaldehyde and ^4He atoms has been obtained from a first-principle calculation of the forces at play. In order to describe the nanoscopic features of HCHO being solvated in a quantum liquid, further Monte Carlo calculations for the system HCHO@He_N with *N* up to 20 have been carried out. The energetics and structure of the systems, as *N* changes, are extensively analyzed, and the excluded volume (“bubble”) created by the inner cage that surrounds the solvated molecule is described and discussed to provide molecular microsolvation details for the title system.

I. Introduction

The past few years have witnessed a tremendous increase of our collective knowledge on the chemical and physical phenomena which play a significant role in the understanding, at the molecular level, of the radiation damage induced in biological molecules. In particular, the experimental discovery of the crucial presence of the free electrons at subexcitation energies, the latter species being the most abundant secondary species following the impact of the primary radiation components,^{1–3} has triggered a host of new studies on a variety of molecular targets, ranging from the individual constituents of DNA and RNA to the larger aggregates like the sugar backbone and the networking of water molecules in the solvent.^{4–6} Thus, although the gas-phase experiments still preserve the advantage of being amenable to detailed observations using mass spectrometric tools, the next challenge for experiments, and for their theoretical interpretation, has been to further analyze the behavior of the interaction of the impinging electrons with the biosystem once the latter is taken down to much lower temperatures that are attainable within cold helium nanodroplets,⁷ which then provide a sort of “gentle” quantum solvent to the biomolecules.

The advent of experiments with such nanodroplets, in fact, has already opened a new area of studies on the nanoscopic features of the microsolvation of several types of simple solutes in a nonconventional quantum partner like bosonic ^4He ,⁸ whereby the solvated dopant could be brought down to the low-temperature conditions estimated to exist for such a solvent (~0.4 K) and, therefore, the effect of the adaptive behavior of the individual adatoms could be related to specific observables of the molecular solute.^{9,10} Thus, the combined employment of both the low-*T* structural effects from the quantum cryostat provided by the droplet and the probing nature of the electron beams on the resonant attachment decays for the biosystems have suggested a new generation of experiments that have extended and strengthened our specific knowledge of the damaging processes in biomolecules.^{11–13}

For a useful analysis of all of the above findings, however, one needs to understand the details during experiments by having acquired some prior, realistic knowledge on how the initial biomolecule is solvated within the nanodroplet and what one expects that the quantum, adaptive environment of the bosonic adatoms will do to accommodate the fairly large presence of the biomolecule embedded in it. Moreover, although the solvation of polyatomic systems by the ^4He solvent has been already studied for molecules such as benzene,^{14,17} tetracene,¹⁵ and phthalocyanine,¹⁶ such calculations have usually involved ad hoc procedures based on the approximation of a nonrotating molecule and of an empirical or, in the case of benzene, not very accurate ab initio interaction potential with the He atom. Therefore, an analysis of the solvation which adopts the full Hamiltonian (including rotation of the dopant), and an accurate potential, could provide useful benchmark data when collecting results on light polyatomic molecules in which the rotation energy could be a significant part of the total energy.

To this end, the present study deals with the characterization of the small clusters where, as an initial simple example, a single formaldehyde molecule is embedded in the He droplet. We shall therefore start by generating a realistic potential energy surface (PES) between the molecule and a single ^4He atom, and then, we shall use a quantum Monte Carlo (QMC) approach to obtain structural information and quantitative estimates of the involved energetics and of the ensuing geometric features at the quantum level.

The paper is organized as follows: the next section discusses the computational tools employed to obtain both the ab initio PES and the stochastic quantum observables, while section III describes the results obtained from the embedding of HCHO into droplets of varying size up to 20 He adatoms. Section IV will finally give our present conclusions and indicate the directions of future work.

II. Computational Tools

A. Modeling of the Interaction. Once we move from simple diatomic molecules to small organic dopants, both the calculation of the actual points which generate a given potential energy surface (PES) and the fitting procedure of such points to yield a more flexible analytic form of the latter become more complicated. For what concerns the setting up of the necessary

[†] Part of the “Reinhard Schinke Festschrift”.

^{*} To whom correspondence should be addressed. E-mail: fa.gianturco@caspur.it. Fax: +39-06-49913305.

[‡] University of Rome La Sapienza.

[§] Koç, University.

TABLE 1: Convergence Tests for Different Methods and Basis Sets for the Systems HCHO–He^a

	HCHO–He (R, θ, φ)		
	3.2, 180, all	3.6, 180, all	3.5, 120, 60
MP2/basis (a)	−10.65	−17.52	−5.59
MP2/basis (b)	−15.24	−19.79	−8.26
MP2/basis (c)	−26.47	−25.93	−15.54
MP2/basis (c)	−27.84	−26.44	−16.42
CCSD(T)/basis (a)	−17.36	−20.62	−9.31
CCSD(T)/basis (b)	−23.52	−23.55	−12.85
CCSD(T)/basis (c)	−38.62	−31.96	−22.49
CCSD(T)/basis (d)	−39.98	−32.54	−23.39

^a Distances in Å, angles in degrees, and energies in cm^{−1}. Basis (a): cc-pVQZ on all partners. Basis (b): cc-pVQZ(HCHO), cc-pV5Z(He). Basis (c): aug-cc-pVQZ on all partners. Basis (d): aug-cc-pV5Z on all partners.

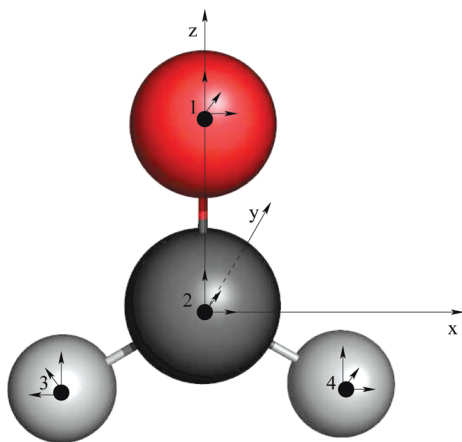


Figure 1. Placement of the four center on the HCHO molecule. The origin of the frame is set on the C atom, the C_2 axis is the z axis, and the xz plane is the molecular plane.

PES, the calculation of a single point requires a higher computational cost, and a larger number of geometries have to be considered in order to realistically span the relevant configurational space in the case of polyatomic dopants.

Specifically, the present PES has been evaluated by carrying out single-point calculations for each chosen orientation for a total of 845 points. A test of different basis sets and different calculation methods has been made as a preliminary step by comparing different results for a small subset of points in order to then select the final choice reported in our work. The results of these tests (reported in Table 1) suggest using the CCSD(T) method with the aug-cc-pvQZ basis set (basis expansion (c) in that table) as the best compromise for the problem at hand. To further enlarge the expansion to the choice of basis (d), in fact, increases the computational time by more than 1 order of magnitude, with only a minor improvement in the details of the PES energetics. All of the single-point calculations have been obtained using the Molpro2002 package,^{19,20} and all of the energy values have been corrected for the BSSE effect with the usual counterpoise procedure of Boys and Bernardi.¹⁸

The final formaldehyde–He PES has been then represented by using the following four-center expansion, where each center corresponds to an atom of the dopant molecule (see Figure 1)

$$V(r, \theta, \varphi) = \sum_{k=1}^4 V^{(k)}(r_k, \hat{\mathbf{r}}_k) \quad (1)$$

and each term $V^{(k)}$ is fitted in turn using the functional form

$$V^{(k)} = e^{-\beta_k r_k} \sum_{n=0}^N \sum_{l=0}^L \sum_m r_k^n \Omega_{lm}(\theta_k, \varphi_k) c_{nlm}^{(k)} + \frac{c_6^{(k)} f_6^{(k)}}{r_k^6} + \frac{c_8^{(k)} f_8^{(k)}}{r_k^8} \quad (2)$$

where the Ω_{lm} are symmetry-adapted real linear combinations of spherical harmonics and the f_N coefficients are the Tang–Toennies damping factors.²¹ The coefficients $c_{nlm}^{(k)}$, $c_6^{(k)}$, and $c_8^{(k)}$ and the β_k parameters have been provided by a numerical procedure based on the well-known Levenberg–Marquardt prescription.²²

In the fitting procedure, we have used values of N and L equal to 1 and 6, respectively, for the oxygen center, 2 and 4 for the carbon center, and 2 and 4 for the two hydrogen centers, which are equivalent by symmetry and have the same parameters. The fit has been carried out by weighting the raw points which have $V > 300$ cm^{−1} with a $1/|V|$ function. The fitted form follows well the ab initio raw points with a standard deviation $\sigma = 1.45$ cm^{−1}. A pictorial view of the potential is given in the three panels of Figure 2, where the isolines correspond to different energy values, also reported in it. All of the fitting parameters and the full routine for generating the present interaction potential are available upon request from the authors.

As one can see from the data in the figure, the deepest attractive well is located on the molecular plane at $\theta \approx 75^\circ$ and at a distance of 3.5 Å; the corresponding value for the energy is about -48 cm^{−1}. By looking at Figure 2, we can therefore identify two main contributions to that energy; the first is the interaction of the He atom with the C=O group located along the vertical axis, while the other is the interaction of He with the H atoms away from that axis. This behavior could be better understood by looking at the charge distribution on the HCHO components, which comes out of a standard Mulliken analysis; a single-point calculation was performed for it with the B3LYP-DFT model and using the 6-311++G** basis set within the Gaussian03 suite of codes.²³ It yielded the following partial charges: -0.24 on the O atom, 0.04 on the C atom, and 0.1 on the H atoms. Although this analysis is only a qualitative estimate of the charge distribution, it gives some idea about the interplay between different contributions to the interaction energies mentioned above; in fact, even if the C=O group is more polarizable than the remaining part of the molecule and, therefore, would have a stronger dispersion interaction with the He atom, it is also an electron-rich and heliophobic region of the HCHO and therefore exhibits marked repulsive effects. On the other hand, the contributions of the interaction of He with the H atoms come from that part of the molecule which is not particularly polarizable, while their exhibition of a partial positive charge helps to establish an attractive interaction with He, as confirmed by the features of the PES of Figure 2.

Once we have obtained the analytical expression for the present potential, we can use it to treat the interactions within small He clusters by choosing a sum of potentials (SOP) approximation to get the potential of an N th component cluster

$$V^{(N)} = \sum_{i=1}^N V(\mathbf{R}_k) + \sum_{i<j} v(r_{ij}) + V_{\text{MB}} \approx \sum_{i=1}^N V(\mathbf{R}_k) + \sum_{i<j} v(r_{ij}) \quad (3)$$

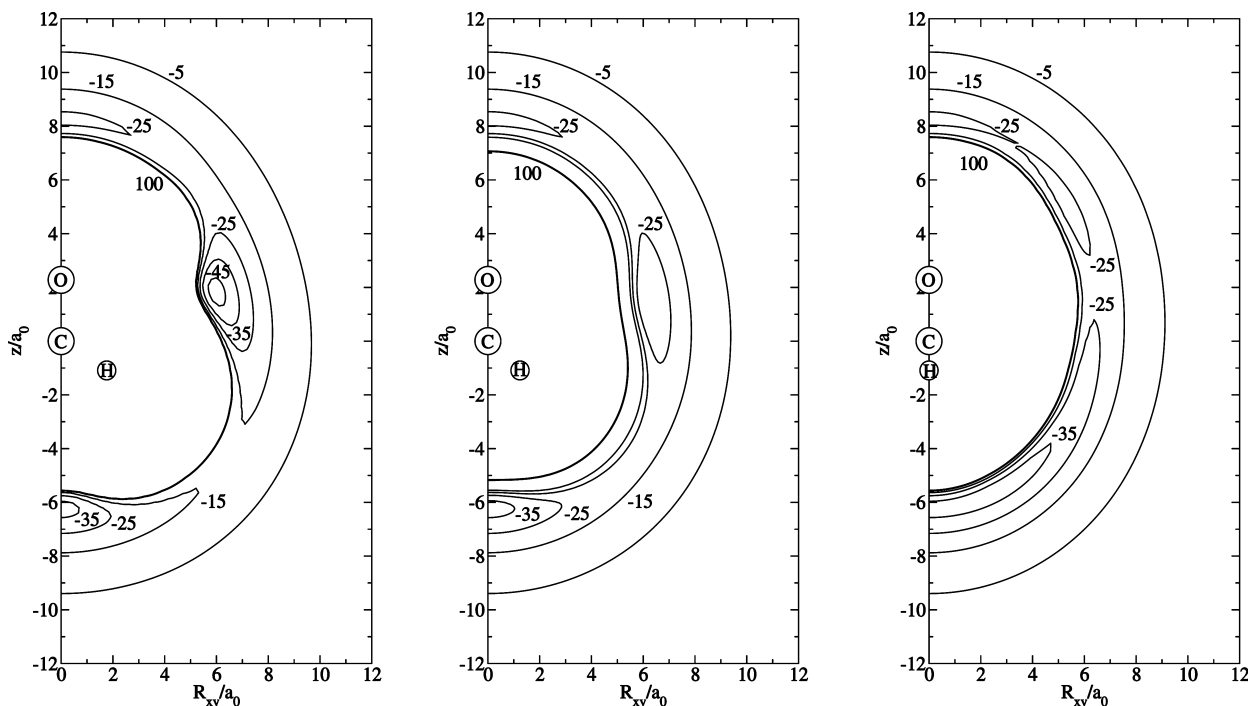


Figure 2. 2D representation of the HCHO–He potential at $\phi = 0, 45,$ and 90° going from left to right. Energy units are in cm^{-1} , and the values are given along representative isoenergetic lines.

where $V^{(N)}$ is the cluster total potential, V is the HCHO–He potential, v is the He–He potential (for which we have used the Aziz expression²⁴), and V_{MB} is the neglected many-body contribution. Disregarding these contributions has been found by us, and many others, not to change the magnitude and the shape of the total cluster potential; therefore, several earlier works have successfully used this kind of approximation.^{25,26} We have also used it in the present calculations.

B. Quantum Monte Carlo Method. In our implementation of the QMC method, we have combined an initial variational approach (variational Monte Carlo, VMC), that optimizes the parameters of the chosen trial wave function with respect to the variance of the mean of the local energy with a diffusion Monte Carlo (DMC) procedure. The implementation of such schemes is similar to the one discussed in one of our recent publications,²⁷ with small changes relating to the presence of a polyatomic molecule as a dopant species within the small clusters. Hence, (1) by following what was discussed in refs 14 and 17, the He–impurity trial wave function is expressed as a product of atom–atom spherical contributions of the following type

$$\log \psi_{\text{Imp-He}}^T = - \sum_i \left(\frac{p_5^{(i)}}{R_i^5} + p_1^{(i)} R_i \right) \quad (4)$$

where i labels the selected atoms of the dopant and R_i is the distance between the i th molecular atom and one of the He atoms. (2) The rotational sampling during the simulation has been carried out by using the quaternionic formulation of rotation as suggested in ref 28. (3) The rotational energy of the impurity is taken into account during the local energy evaluation by using the following operator

$$T_{\text{rot}} = -B_x \frac{\partial^2}{\partial \phi_x^2} - B_y \frac{\partial^2}{\partial \phi_y^2} - B_z \frac{\partial^2}{\partial \phi_z^2} \quad (5)$$

where the parameters B_i are the rotational constants of the molecule along the reference axis of the frame which diagonalizes the inertia tensor and the corresponding ϕ_i angles are rotation angles about the chosen i th reference axis. (4) The He–He trial wave function is not selected entirely as the usual Jastrow-type function,²⁹ but it contains fewer terms in order to save computational time without affecting the method’s final accuracy

$$\log \psi_{\text{He-He}}^T = - \left(\frac{p_5}{r_{ij}^5} + p_1 r_{ij} \right) \quad (6)$$

where r_{ij} is obviously the distance between the i th and the j th He atoms.

The VMC calculations have been divided into 30 blocks of 5000 time steps along which the Metropolis algorithm³⁰ was used, while for DMC we have chosen an important sampling implementation of it, and we have carried out two series of 40 blocks per 5000 time steps, with one calculation using a constant population branching (CPB) algorithm³¹ and the second one using a variable population³² (VPB) in order to compare and validate the two series of results. In both cases, the Monte Carlo scheme was set to employ a total of 2000 walkers.

III. Results and Discussion

The QMC calculations have been carried out for the series of clusters from $N = 1$ up to 20. The chosen simulation time was found to be long enough to ensure obtaining convergence to the “exact” ground-state energies of the various clusters, as demonstrated by the error values being always lower than 1% of the total binding energies.

A. HCHO–He Complex. For the smallest complex with $N = 1$, the binding energy was found to be $-9.497(7) \text{ cm}^{-1}$ when using the CPB algorithm, while it turned out to be $-9.60(4) \text{ cm}^{-1}$ when using the VPB approach. The fact that they are very close values confirms the accuracy of the present calculations.

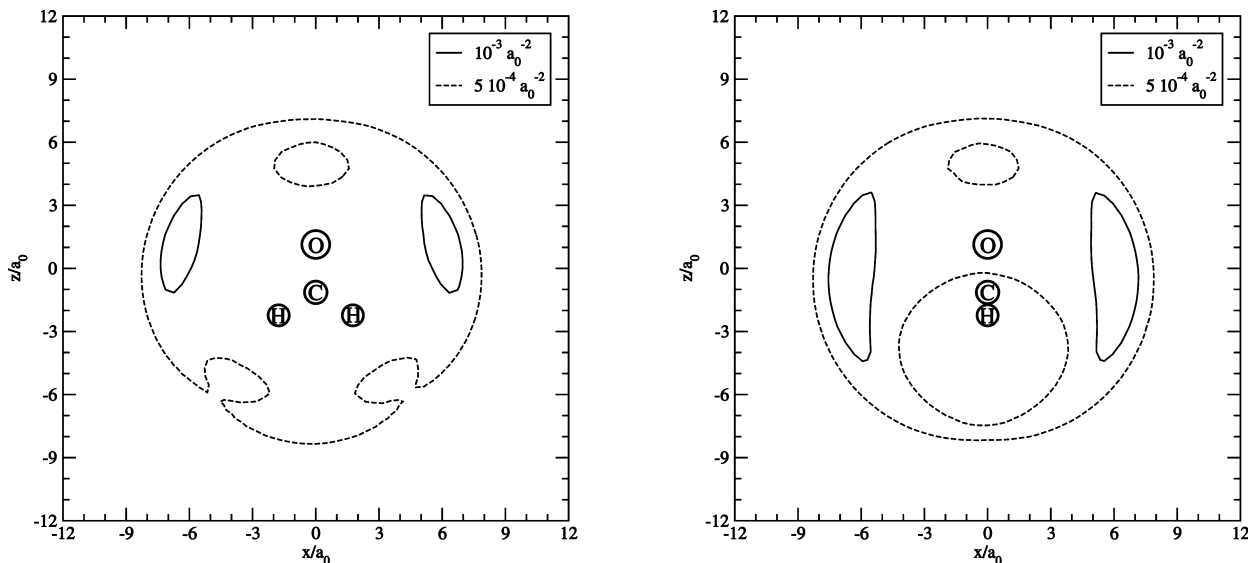


Figure 3. Projection of the total He density probability for the complex HCHO–He onto the Cartesian planes xz (left panel) and yz (right panel). The distances are in units of bohr (a_0).

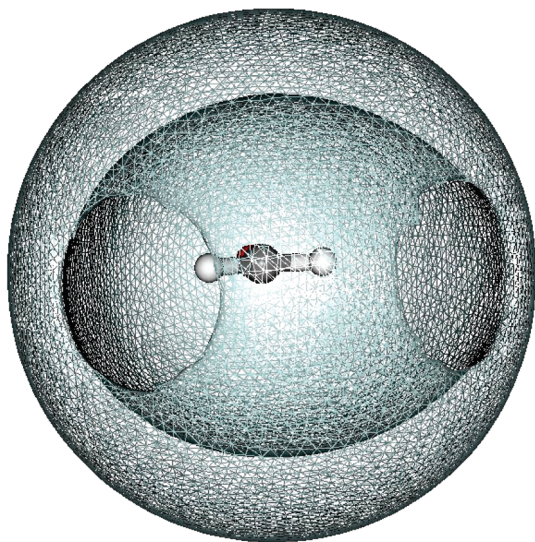


Figure 4. 3D single-atom He density for the HCHO–He complex; including the outermost isosurface value is $4 \times 10^{-4} a_0^{-3}$, which corresponds to the $73.89 \pm 0.08\%$ of the He total density. The solvated molecule is perpendicular to the plane of the figure, with the H atoms pointing outward. The solvent density is evaluated with the CPB algorithm, and the varying percentage of He atomic densities included is obtained with the algorithm described in section IV.

Such data yield a zero-point energy (ZPE) value of about 38 cm^{-1} , which is almost 80% of the deepest potential well. This indicates that the quantum features of this systems are very marked and that a “classical” view which takes the He adatoms to be points localized at the potential minima is rather misleading since the ZPE effects are bound to delocalize the solvent atoms and modify the structural picture. Figure 3 shows the two-dimensional (2D) He distribution obtained as a projection on the Cartesian planes xz , yz . As we can see from that figure, the He density profile follows fairly closely the potential energy landscape, with the major portion of the He solvent atom, which is located along the carbonyl, at the oxygen side of the dopant and between the two H atoms. A sort of “He vacancy” occurs instead along the two CH bond, which are, therefore, heliophobic regions. This can be better seen in Figure 4, where the three-dimensional (3D) density of the He atom exhibits a marked dip close to the locations of the hydrogen atoms.

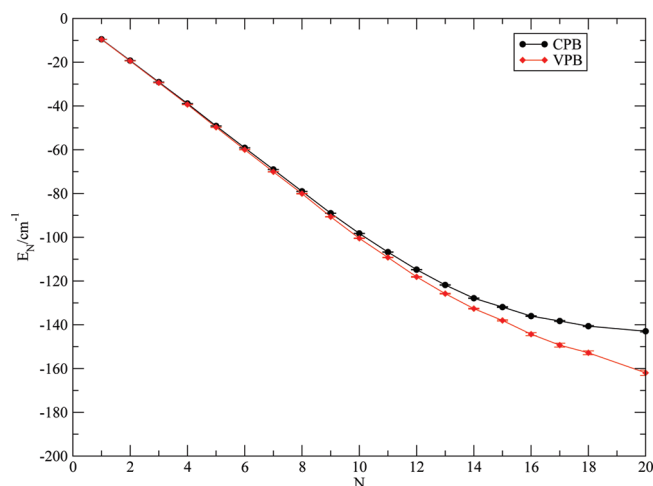


Figure 5. Total energy versus N . The two sets represent results for the constant population branching (circles) and the variable population branching (diamonds). Energies are in cm^{-1} . Error bar are within the symbols’ size.

B. Larger Clusters. A plot of the total energies, calculated using both the CPB and the VPB algorithms is presented in Figure 5 up to $N = 20$. The two series of results are slightly different, with the VPB binding energies being larger than the CPB ones; in fact, the CPB scheme usually gives results with smaller errors with respect to the VPB data since the latter approach is less precise but more effective in providing the total energies. This behavior has been seen consistently in the several tests that we have carried out for different He complexes containing a molecular or atomic impurity and for which the “exact” discrete variable representation (DVR) results were also available for comparison.³³ It is therefore reasonable to see in the figure that the energy differences between the two schemes increase with N .

The series of the total energies is found to be almost linear up to $N = 9$, after which value both curves become smoother and the energy gain per adatom gets smaller. This can be better appreciated if we look at Figure 6, in which the single-atom evaporation energies (ΔE_N) are reported

$$\Delta E_N = E_N - E_{N+1} \quad (7)$$

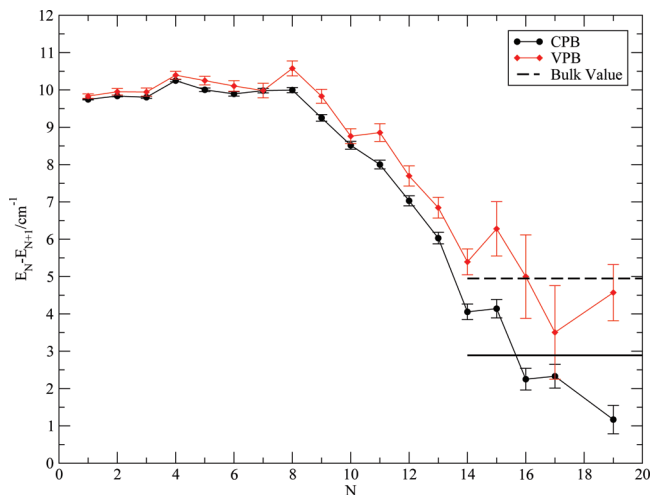


Figure 6. Single-atom evaporation energy versus N . Both CPB (circles) and VPB (diamonds) results are shown with the correspondent error bars. The bulk value has been taken from ref 34. The large cluster value of ref 36 is given by the solid line. Energies are in cm^{-1} .

The decreasing value of the evaporation energies that starts with the case of $N = 9$ is clearly shown. We further see that after this cluster size, the energy goes smoothly down and tends to reach a sort of N -independent bulk value. We can compare this value with the known one for a macroscopic sample of liquid He; it was found to be around 5 cm^{-1} ³⁴ when an earlier Aziz He–He potential is used.³⁵ A more recent calculation for a pure He cluster of 240 atoms that uses the same potential as ours gives a single-particle energy equal to -2.89 cm^{-1} ³⁶ for a cluster of that size, that is, not yet at the bulk size. It is important to emphasize here the difference between the present kind of “gentle” dopant given by formaldehyde and a more strongly perturbing one such as the alkali metal ions.²⁶ In the latter situation, in fact, the plots of the computed evaporation energies present highly marked jumps which correspond to reaching configurations with highly structured, and more dense, He arrangements around the dopant; the case of formaldehyde, on the contrary, is more similar to that of the halide anions³⁷ in which the evaporative energies show a monotonic behavior when progressing toward the larger N values and the surrounding He solvent provides essentially a liquid environment.

The absence of structuring effects is also confirmed by plotting the HCHO–He distance probability densities, as done in Figure 7, in which different cluster sizes are compared. The shape of the distribution does not change much with N for all of the examined sizes, with the exception of $N = 16$, in which, however, only a small shift of the most probable distance value occurs. We also see a more extended tail of the distribution in the range of the larger distances; it indicates that the spatial region closer to the dopant is now completely filled and therefore the additional atoms have to be placed further out with respect to the impurity. On the other hand, the absence of a new maximum also indicates that these outer atoms are forming a sort of continuous “layering” around the dopant and not a new, discontinuous shell; rapid exchange of indistinguishable bosonic partners therefore further eliminates any structuring effect.

Figure 8 additionally shows the distribution of the cosine of the angle α between the dopant and any two solvent atoms within the cluster. As one can see in this figure, there are two clearly distinguishable regions of behavior for this angle, one in which a marked peak in the distribution is very visible and another in which a smoothly constant distribution is present, one which increases in value as N becomes larger. The former

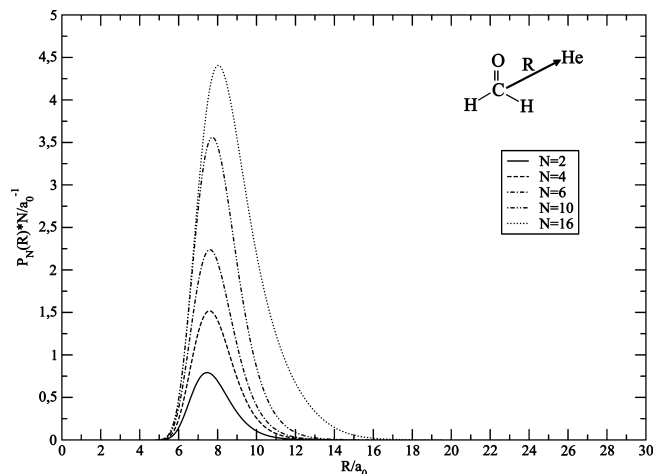


Figure 7. Radial probability densities for the HCHO–He distance obtained in different sizes of clusters. The values have been obtained using the CPB algorithm. Distances are in bohr (a_0).

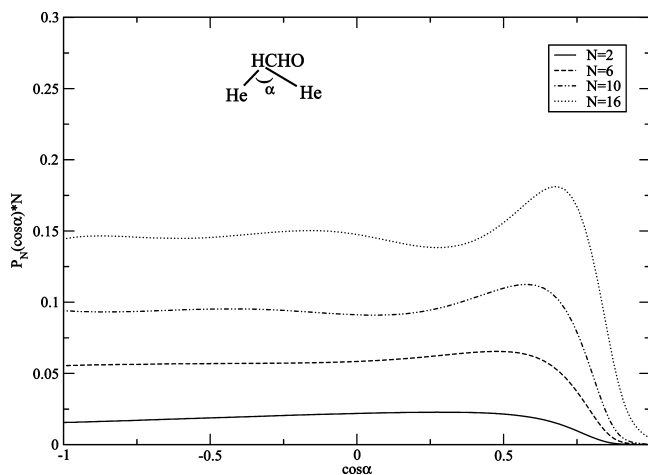


Figure 8. Probability densities of $\cos \alpha$, with α defined as the angle between any two He atoms and the dopant. Different cluster sizes are shown. The distributions have been obtained using the CPB algorithm.³¹

corresponds to a more probable angle $\alpha \approx 55^\circ$ that refers to He atoms which are closer to the impurity, while the latter is the contribution of the solvent’s external layers.

By summarizing the results that we have discussed thus far, we can say that the initial He adatoms place themselves within the cluster around the impurity by forming a liquid-like layer in which we can however still observe fluctuations in the probability distribution for the impurity–He distance ($R \approx 7.5 a_0$) and for the He–impurity–He angle ($\alpha \approx 55^\circ$). This happens more markedly up to $N = 9$, while when adding new atoms to the cluster, we observe a decrease in the evaporation energies, indicating that the new adatoms are more weakly bound to the system, and a shifting of the more probable distances toward larger values, where the probability distributions of the α angle defined before now yield higher probability also for $\alpha > 55^\circ$. A pictorial view of the density distribution of the solvent atoms in one of the representative clusters description is given in Figure 9, where one can clearly identify the “bubble” area associated with essentially no density of solvent adatoms. It is also interesting to note that an overall probability density that only includes about 50% of the present adatoms is already fully surrounding the dopant molecule.

Because of the liquid-like features of the He solvent in the present system, it is harder to characterize the solvation process

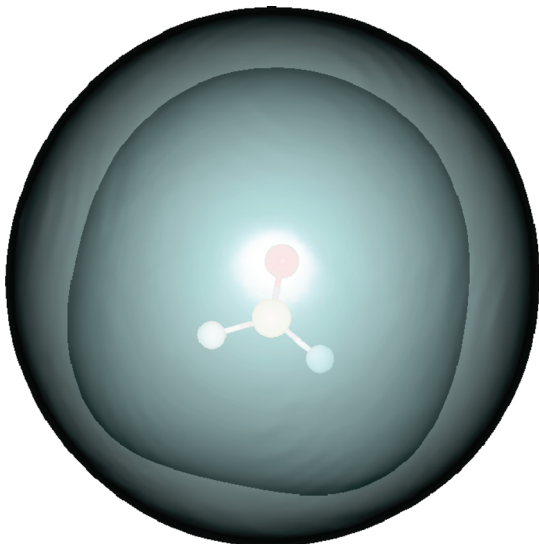


Figure 9. Three-dimensional representation of the HCHO@He₁₀ system. The outermost isosurface value is $\rho = 2.410^{-4} \text{ a}_0^{-3}$, which includes $48.13 \pm 0.11\%$ of the total density of He atoms. The density distribution is obtained using the CPB algorithm,³¹ while the percentage of He probability density is evaluated as described in section IV.

along the series of the clusters, as was done instead for the alkali metal cations.²⁶ It is therefore preferable to describe the solvation process by using a procedure similar to that adopted in one of our earlier works;³⁹ we select a certain number of regions surrounding the dopant and measure in them the corresponding “local” density of the solvent atoms as sector-integrated values.³⁹ In this way, we can identify for each value of N which of the selected regions is helium-rich and which one is helium-poor. Figure 10 shows that for the smaller clusters ($N \leq 5$), the He-rich region is really the one along the main molecular axis, that is, the areas between the oxygen and the H atoms. The near-oxygen and near-hydrogen areas remain He-poor regions. As N increases, however, and as one qualitatively expects, the adatoms tend to adapt to the molecular shape in an uniform way, thereby yielding similar densities in each of the sectors. This can be qualitatively explained by looking at the overall potential given by Figure 2; the side-region to the carbonyl is the one in which the strongest attractive minima occur, and for this reason, it remains the one with the higher probabilities in terms of He presence. On the other hand, the remaining regions are characterized by less attractive PES behavior and are therefore less populated during the cluster growth, at least for the smaller clusters. Furthermore, the growth of the clusters suggests the permanence of the liquid-like structure of the solvent and therefore the near-uniform distribution of the adatom probability densities around the polyatomic dopant.

IV. Assessing the “Bubble” Features

One of the interesting outcomes of our calculations for this systems is the rather large empty volume surrounding the dopant, as pictorially shown in Figure 9. It would thus be interesting to relate this feature to both a spatial region that defines a sort of excluded volume in which the HCHO–He repulsive potential is greater than a preselected value and to the one delimited by the empirical van der Waals (VdW) radii of the molecular atoms. The additional method which we have also used in order to yield this quantity is the Monte-Carlo-obtained evaluation of the expectation value of the step function (θ) within a uniform probability function.⁴⁰

$$V(\omega) = \int_{\Omega} \theta(x) dV = V(\Omega)\langle\theta\rangle \approx \frac{V(\Omega)}{N} \sum_{i=1}^N \theta(x_i) \quad (8)$$

where Ω is a preselected spatial domain, ω is the volume of the cavity, and θ is the step function, which is equal to 1 in ω and 0 elsewhere. In other words, the volume of ω is obtained as the product of the domain volume ($V(\Omega)$) times the frequency of the occurrences of the walkers in ω during the random walk.

A series of calculations with 3000 walkers with 5000 time steps per 40 blocks in a domain of $V = 4096 \text{ a}_0^3$, have been carried out for the whole series of clusters ($N = 1-20$). The regions ω have been respectively defined as the one delimited either by the VdW radii or by the interaction regions where the potential value is greater than 200, 300, or 350 cm^{-1} and the one in which DMC He density is completely 0 or, in other words, where no walkers have He atoms in such a region.

A plot of the various computed volumes is presented in Figure 11. As we can see, the actually computed volumes decrease as N increases up to $N = 6$, after which they reach an almost constant value. This can be explained by noting that the less attractive part of the interaction causes in it a lower He density, and then, it exhibits a correspondingly thinner He layer. When the He adatoms eventually completely fill the region surrounding the impurity, the surrounding volume becomes essentially a constant for all of the examined values of N . In the same figure, constant values of volumes extracted from the HCHO–He PES and from VdW radii are also shown; as one can see, the latter estimates usually provide a larger excluded volume.⁴¹ At the same time, when we wish to get a more realistic, albeit still size-independent, estimate of the bubble volume, we have to consider a more repulsive threshold for the exclusion provided by the potential. This can also be seen in Table 2 where the four types of volume are compared and their corresponding average distances from the dopant, obtained from $(3V/4\pi)^{(1/3)}$, are also given.

It is interesting to note here that the results from the various ways in which we estimate the size of the surrounding cavity volume (the “bubble” created by the dopant) indicate consistently a fairly large cavity size; this means that the impurity can be more directly seen by other solvated species that could be in the droplet, which are, in turn, able to move closer to the primary dopant without much effective screening by the solvent adatoms. In other words, the solvated molecules are easier to be reached from other interacting species eventually present, while this does not occur that easily for strong interacting impurities such as cations, which are more strongly caged by more closely packed He atoms and are less readily reached by additional dopants.⁴²

V. Present Conclusions

The results discussed and analyzed in the previous sections of this paper deal with the computational assessment of the structural behavior of a small, polyatomic molecular dopant within the confined volumes created by the cold environment of bosonic He clusters, where the number of adatoms has been limited to about 20 ⁴He partners.

The theoretical and computational issues from such a study can be briefly summarized as follows:

(1) The initial task of such analysis invariably involves the determination of the correct force fields for the dopant molecule placed within the ⁴He clusters or droplets. This was achieved in the present study by using and entirely ab initio, all-electron

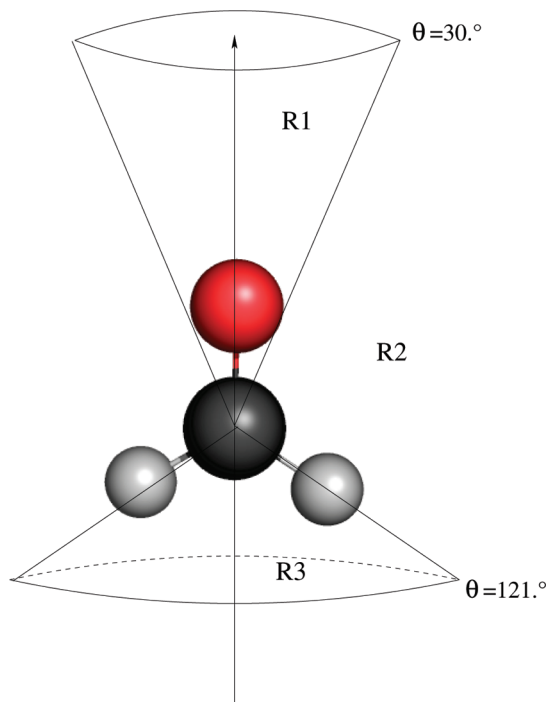
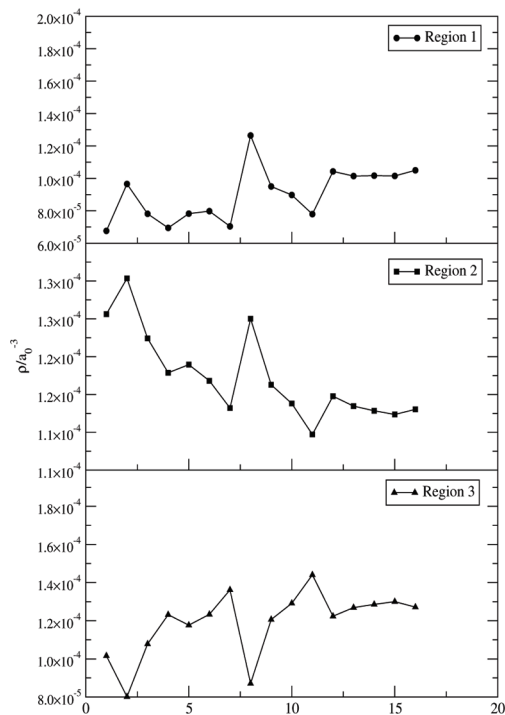


Figure 10. Plot of ρ_i for $i = 1-3$. The reported regions in the three panels on the left are defined in the right figure sector. Each point of each panel, once integrated over its sector volume, yields the corresponding fraction of He atoms in that sector.

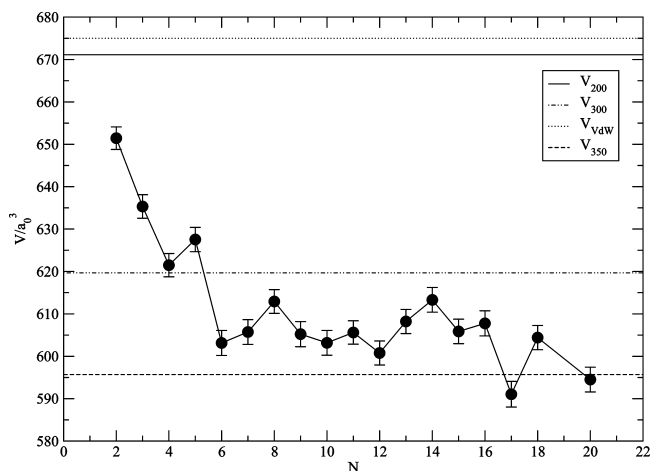


Figure 11. Excluded volumes versus N . The VdW radii are taken from ref 38. Units are bohr³ (a_0^3).

TABLE 2: Comparison of the Monte-Carlo-Computed Volume of the Cluster with $N = 18$, the VdW Volumes, and the Volumes in Which the Potential Cut Is Greater than Either 200 or 300, along with the Average Radius of the Shown Cavities^a

	V/a_0^3	r_{eff}/a_0
HCHO@He ₁₈	604.4(2.9)	5.24
V_{200}	671.1(2.9)	5.4
V_{300}	619.7(2.6)	5.3
V_{350}	595.7(2.7)	5.2
V_{VdW}	675.0(2.8)	5.4

^a All quantities are in a_0 units.

approach beyond the Hartree–Fock level of calculations. The latter interaction was then employed to map around the formaldehyde molecule the energy distribution associated with a single ⁴He as a probing species.

(2) The analytic representation of the ensuing grid of ab initio points was also an important step of the present analysis. This

was done by employing a physically oriented approach that selects different fitting forms in different regions of space. The final result was a flexible force field that could then be employed in several different contexts, in particular, the full potential form for the actual clusters of interest was then obtained here by employing the sum-of-potentials approximation. The latter has been found to be very realistic when dealing with multiple interactions in weakly coupled N -particle systems as those examined in the present study.

(3) The construction of the 3D spatial configurations of the clusters was then carried out by using a stochastic approach at 0 K, that is, by using both variational and diffusion Monte Carlo treatments (VMC and DMC) in order to obtain the energies and helium density distributions for the series of doped clusters of interest.

(4) The converged, final results have been able to tell us the occurrence of a full solvation of the present dopant into the clusters, the values of their binding energies, and the values of the binding energies of each of the sequentially added ⁴He adatoms along the series of examined small clusters. They have also indicated that the outer layers of the quantum solvent largely maintain their liquid behavior and do not exhibit the appearance of magic numbers or of marked shell structures, which can effectively screen the dopant.

(5) The present calculations are therefore able to show that the solvated molecule is really surrounded by an adaptive, nonclassical solvent which distributes its component adatoms according to the strength of their relative local binding behavior, as seen by the data of Figure 10, but which also maintains a strong nonclassical behavior with large delocalization within the droplet.

(6) Finally, the quantum structure calculations also show that the presence of a nonlinear molecule, despite its smallness and simplicity, already creates inside each cluster a sort of a low-density excluded volume of space representing the effects of

the adaptive interactions between adatoms with respect to the dominant interactions of the ^4He partners with the dopant molecule.

In conclusion, the above results indicate that even a small object like formaldehyde is already capable of providing us with several, and possibly general, indicators that define the micro-solvation process at the nanoscopic level and that can also be used to extend the evaluation to larger dopants. We shall be presenting our findings within the latter context in future publications from our group.

Acknowledgment. We are very grateful to Dr. E. Coccia for his generous help during the preliminary completion of our new code for polyatomic dopants. We also thank the CASPUR Consortium for providing the computational time, together with the High Performance Computing Project from the CINECA consortium. The financial support from the Research Committee of the Science Faculty of the University of Rome "La Sapienza" is also acknowledged. Finally, we wish to thank Professor Paul Scheier, from Innsbruck University, for drawing our attention to their experimental results and to the present problem.

References and Notes

- (1) Boudaiffa, B.; Cloutier, P.; Hunting, D.; Huels, M. A.; Sanche, L. *Science* **2000**, *287*, 1658.
- (2) Panajotovic, R.; Martin, F.; Cloutier, P.; Hunting, D.; Sanche, L. *Radiat. Res.* **2006**, *165*, 452.
- (3) Sanche, L. *Eur. Phys. J. D* **2005**, *35*, 367.
- (4) Bald, I.; Kopyra, J.; Illenberger, E. *Angew. Chem., Int. Ed.* **2006**, *45*, 4851.
- (5) Li, X.; Sevilla, M. D.; Sanche, L. *J. Am. Chem. Soc.* **2003**, *125*, 13668.
- (6) Baccarelli, I.; Gianturco, F. A.; Grandi, A.; Sanna, N.; Bald, I.; Kopyra, J.; Illenberger, E. *J. Am. Chem. Soc.* **2007**, *129*, 6269.
- (7) Toennies, J. P.; Vilesov, A. F. *Angew. Chem., Int. Ed.* **2004**, *43*, 2622.
- (8) Farnik, M.; Toennies, J. P. *J. Chem. Phys.* **2003**, *118*, 4176.
- (9) Paesani, F.; Viel, A.; Gianturco, F. A.; Whaley, B. *Phys. Rev. Lett.* **2003**, *90*, 073401.
- (10) Sebastianelli, F.; Di Paola, C.; Baccarelli, I.; Gianturco, F. A. *J. Chem. Phys.* **2003**, *119*, 8276.
- (11) Denifl, S.; Zappa, F.; Mähr, I.; Lecointre, J.; Rondino, F.; Echt, O.; Märk, T.; Scheier, P. *Eur. Phys. J. D* **2007**, *43*, 117.
- (12) Denifl, S.; Zappa, F.; Mähr, I.; Lecointre, J.; Probst, M.; Echt, O.; Märk, T.; Scheier, P. *Phys. Rev. Lett.* **2006**, *97*, 043201.
- (13) Feil, S.; Gluch, K.; Denifl, S.; Zappa, F.; Echt, O.; Scheier, P.; Märk, T. *Int. J. Mass Spectrom.* **2006**, *252*, 166.
- (14) Huang, P.; Whaley, K. B. *Phys. Rev. B* **2003**, *67*, 155419.
- (15) F Whitley, H.; Huang, P.; Kwon, Y.; Whaley, K. B. *J. Chem. Phys.* **2005**, *123*, 54307.
- (16) Whitley, H. D.; DuBois, J. L.; Whaley, K. B. *J. Chem. Phys.* **2009**, *131*, 124514.
- (17) Kwon, Y.; Whaley, K. B. *J. Chem. Phys.* **2000**, *114*, 3163.
- (18) Boys, S. F.; Bernardi, F. *Mol. Phys.* **1970**, *19*, 553.
- (19) *MOLPRO*, a package of ab initio programs written by Werner, H.-J. Knowles, P. J. with contributions from others; for more information, see: [www page http://www.molpro.net](http://www.molpro.net).
- (20) Hampel, C.; Peterson, K.; Werner, H.-J. *Chem. Phys. Lett.* **1992**, *190*, 1.
- (21) Tang, K. T.; Peter Toennies, J. *J. Chem. Phys.* **1984**, *80*, 3726.
- (22) Press, W. H.; Teukolosky, S. A.; Vetterling, W. T.; Flannery, B. P. *Numerical recipes in fortran 77*, 2nd ed.; Cambridge University Press: Cambridge, U.K., 1992.
- (23) Frisch, M. J.; Trucks, G. W.; Schlegel, H. B.; Scuseria, G. E.; Robb, M. A.; Cheeseman, J. R.; Montgomery, J. A., Jr.; Vreven, T.; Kudin, K. N.; Burant, J. C.; Millam, J. M.; Iyengar, S. S.; Tomasi, J.; Barone, V.; Mennucci, B.; Cossi, M.; Scalmani, G.; Rega, N.; Petersson, G. A.; Nakatsuji, H.; Hada, M.; Ehara, M.; Toyota, K.; Fukuda, R.; Hasegawa, J.; Ishida, M.; Nakajima, T.; Honda, Y.; Kitao, O.; Nakai, H.; Klene, M.; Li, X.; Knox, J. E.; Hratchian, H. P.; Cross, J. B.; Bakken, V.; Adamo, C.; Jaramillo, J.; Gomperts, R.; Stratmann, R. E.; Yazyev, O.; Austin, A. J.; Cammi, R.; Pomelli, C.; Ochterski, J. W.; Ayala, P. Y.; Morokuma, K.; Voth, G. A.; Salvador, P.; Dannenberg, J. J.; Zakrzewski, V. G.; Dapprich, S.; Daniels, A. D.; Strain, M. C.; Farkas, O.; Malick, D. K.; Rabuck, A. D.; Raghavachari, K.; Foresman, J. B.; Ortiz, J. V.; Cui, Q.; Baboul, A. G.; Clifford, S.; Cioslowski, J.; Stefanov, B. B.; Liu, G.; Liashenko, A.; Piskorz, P.; Komaromi, I.; Martin, R. L.; Fox, D. J.; Keith, T.; Al-Laham, M. A.; Peng, C. Y.; Nanayakkara, A.; Challacombe, M.; Gill, P. M. W.; Johnson, B.; Chen, W.; Wong, M. W.; Gonzalez, C.; Pople, J. A. *Gaussian 03*, revision C.02; Gaussian, Inc.: Wallingford, CT, 2004.
- (24) Aziz, R. A.; Mc Court, F. R.; Wond, C. C. K. *Mol. Phys.* **1987**, *61*, 1487.
- (25) Marinetti, F.; Bodo, E.; Gianturco, F. A. *ChemPhysChem* **2007**, *8*, 93.
- (26) Coccia, E.; Bodo, E.; Marinetti, F.; Gianturco, F. A.; Yurtsever, E.; Yurtsever, M.; Yildirim, E. *J. Chem. Phys.* **2007**, *126*, 124319.
- (27) Coccia, E.; Marinetti, F.; Bodo, E.; Gianturco, F. A. *J. Chem. Phys.* **2008**, *128*, 134511, and references therein.
- (28) Benoit, D. M.; Clary, D. C. *J. Chem. Phys.* **2000**, *113*, 5193.
- (29) Jastrow, R. *Phys. Rev.* **1955**, *98*, 1479.
- (30) Bressanini, D.; Morosi, G.; Mella, M. *J. Chem. Phys.* **2002**, *116*, 5345.
- (31) Assaraf, R.; Caffarel, M.; Khelif, A. *Phys. Rev. E* **2000**, *61*, 4566.
- (32) Blume, D.; Lewerenz, M.; Huisken, F.; Kaloudis, M. *J. Chem. Phys.* **1996**, *105*, 8666.
- (33) Coccia, E.; Marinetti, F.; Gianturco, F. A. Private communication.
- (34) Pandharipande, V. R.; Pieper, S. C.; Wiringa, R. B. *Phys. Rev. B* **1986**, *34*, 4571.
- (35) Aziz, R. A.; Nain, V. P. S.; Carley, J. S.; Taylor, W. L.; McConville, G. T. *J. Chem. Phys.* **1979**, *70*, 4330.
- (36) Rama Krishna, M. V.; Whaley, K. B. *J. Chem. Phys.* **1990**, *93*, 6738.
- (37) Coccia, E.; Marinetti, F.; Bodo, E.; Gianturco, F. A. *ChemPhysChem* **2008**, *9*, 1323.
- (38) Bondi, A. *J. Phys. Chem.* **1964**, *68*, 441.
- (39) Piccarreta, C.; Gianturco, F. A. *Eur. Phys. J. D* **2006**, *37*, 93.
- (40) Press, W.; Teukolosky, S.; Flannery, W. V. B. *Numerical Recipes in Fortran 77*, 2nd ed.; Cambridge University Press: Cambridge, U.K., 2003.
- (41) N.C.C. Comparison and B. Database, NIST Standard Reference, Database Number 101, Release 14; Johnson, R. D., III, Ed.; National Institute of Standards and Technology: Gaithersburg, MD, <http://srdata.nist.gov/cccbdb> (2006).
- (42) Marinetti, F.; Bodo, E.; Gianturco, F. A. *ChemPhysChem* **2007**, *8*, 93.